Communication

The Effectiveness of Hot Isostatic Pressing for Closing Porosity in Titanium Parts Manufactured by Selective Electron Beam Melting

SAMUEL TAMMAS-WILLIAMS, PHILIP J. WITHERS, IAIN TODD, and PHILIP B. PRANGNELL

Ti-6Al-4V parts, produced by selective electron beam melting additive manufacturing, have been studied by X-ray computed tomography (XCT) to track pore closure during a standard hot isostatic pressing (HIPing) cycle. Comparison of repeated XCT scans before and after HIPing, on worst-case samples with different geometries, confirmed that all internal porosity was shrunk to below the resolution limit of the equipment used (~5 μm) following the HIPing cycle, apart from defects with surface connected ligaments.

DOI: 10.1007/s11661-016-3429-3

Additive manufacturing (AM) processes allow components to be directly produced from CAD models by dividing them into thin 2D slices, which are built sequentially on top of one another. In powder bed processes, such as selective electron beam melting (SEBM), material is added by spreading a thin layer of powder across the build area. A rapidly moving focused electron beam is then used to selectively melt each powder layer, to densify the required cross-section profile, and fuse it to the previously deposited layer.[1,2] A distinguishing feature of the SEBM process is that the whole build takes place at an elevated controlled temperature that is maintained by pre-heating through rapid scanning of the defocused electron beam across the powder bed prior to melting each layer, which reduces the build-up of residual stresses in the part.[1]

The static mechanical properties of Ti-6Al-4V components produced by SEBM have been shown to be comparable to those of conventional wrought material, but the high-cycle fatigue life can exhibit considerable scatter even when testing polished samples.[1,2] This scatter is primarily caused by the presence of pores in the consolidated material, which acts as fatigue crack initiation sites, due to the stress concentration they generate in the surrounding material.[3]

Three types of defect with separate origins and appearance have been previously identified in Ti-6Al-4V material produced by the Arcam SEBM process.[4–10] Most commonly observed are gas pores, which are caused by small bubbles of argon trapped inside the feedstock that arises as an artifact of the atomization process used to produce the powder. If the argon is unable to escape the melt pool during the SEBM process, this results in small (5 to 100 μm) near spherical voids in the solid material.[4–7] More irregular lack of fusion defects are caused by the electron beam failing to fully melt and consolidate the powder layer.[4,7–9] Thirdly, and more rarely, in samples built with older generation machines and control software,[4] or with a non-optimum-reduced energy density,[10] tunnel defects that span multiple deposited layers have been observed. The origin of such defects has been elegantly simulated using lattice Boltzmann modeling by Bauereiß *et al.*[10] who demonstrated that they develop in a layer-wise deposition process when capillary and wetting effects overcome gravitational forces. This leads to the melted powder tracks separating by beading up of the liquid, rather than it filling in large voids present in the preceding layer.[10] This work has shown that tunnel defects are produced under conditions where insufficient beam line energy is applied.

Hot isostatic pressing (HIPing) is a well-established method for healing internal porosity in titanium castings and has been widely used to significantly increase fatigue life in critical components.[11] HIPing involves the simultaneous application of high temperatures and pressures, *via* an inert gas, to a component. At the reduced yield stress and higher diffusion rates associated with high temperatures, the applied pressure leads to pore collapse by small scale plastic flow and material transport that under ideal conditions also bonds the pore interface.[12] Recently, X-ray computed tomography (XCT) has been used to analyze cast Ti-6Al-4V samples, before and after HIPing, and it was found that even the largest internal porosity was closed to below the resolution limit of the equipment used (20 μm).[13] Some pores were found to persist following the HIP cycle, but these were located close to the sample surfaces and it was suggested that micro-cracks, too small to be detected by XCT, connected them to the exterior. HIPing is also now being widely implemented by industry to remove porosity from components produced

SAMUEL TAMMAS-WILLIAMS, formerly Ph.D. Student with the School of Materials, University of Manchester, Manchester M13 9PL, UK, and also Visiting Student with the Department of Materials Science and Engineering, University of Sheffield, Sheffield S1 3JD, UK, is now Postdoctoral Research Associate with the Department of Materials Science and Engineering, University of Sheffield. Contact e-mail: s.tammas-williams@sheffield.ac.uk IAIN TODD, Professor, is with the Department of Materials Science and Engineering, University of Sheffield. PHILIP J. WITHERS and PHILIP. B. PRANGNELL, Professors, are with the School of Materials, University of Manchester.

Manuscript submitted July 9, 2015.
Article published online March 16, 2016

by SEBM before putting them into service. Metallographic examination of HIPed SEBM samples has revealed remnants of pores that have significantly reduced in size but where the contacting interface area generated by their collapse has not always fully bonded.[4] Despite the presence of remnant porosity, mechanical testing has confirmed an improvement in the high-cycle fatigue life following HIPing.[14,15] However, to date, there have been no studies reported that have quantified the efficiency of pore closure in HIPed SEBM parts with statistically significant data.

In this work, XCT has been used to characterize the porosity seen in SEBM Ti-6Al-4V samples before and after the application of a standard HIP cycle. The non-destructive nature of XCT has allowed the effectiveness of post-build HIPing to be studied by directly comparing the behavior of a large number of individual pores and by quantifying their net change in volume and size. In order to confirm that HIPing is capable of removing even "worst-case scenario" largest defects, the samples used in this study were produced using an early variant of the SEBM process and control software. Specifically, they were manufactured using an Arcam S12 machine and a now superseded control system, which prior experience has shown produced samples containing significantly more porosity than when manufacturing using up-to-date procedures. In particular, with this now obsolete setup, the build conditions were known to produce large tunnel defects near sample surfaces. A range of sample build geometries were also chosen to provide different levels of tunnel defects, as well as the more typical gas pores and lack of fusion defects seen in samples produced with the most up-to-date procedures.

In common with the current methodology, in the Arcam machine, the melting stage takes place in two steps. First, a contour strategy is used to melt the outline of each 2D section, before a hatching strategy fills in the section area with continuous linear beam rastering in a forwards and backwards 'snaking' pattern. To avoid overheating the already hot region where a hatching track turns back on itself, a turning function increases the beam speed, while keeping the energy constant. The hatching speed is also increased when melting any overhanging section to compensate for the insulating effect of the powder bed. More details on the melting strategies employed are available in References 4 through 7 and 16.

Each of the seven sample geometries investigated (as shown in Figure 1) was manufactured in a single build cycle with gas-atomized Ti-6Al-4V powder as the feedstock. These small samples were designed to have the same maximum X-ray beam path in a single plane (15 mm), which allowed the same XCT settings (voltage, power, beam filter, *etc.*) to be used when first scanning the entire volume of each sample at a lower resolution. To enable higher resolution scanning, a second cuboid, with identical geometry to S1, was built and machined into a smaller cylinder (~1.7 mm diameter in x–y plane, 10 mm length in z direction) taken from near the sample edge. XCT scanning was carried out at the Henry Moseley X-ray Imaging Facility at the University of Manchester. The full samples were scanned using a Nikon Metrology 225/320 kV Custom Bay system, while the machined cylinder was scanned using a Zeiss Xradia Versa 500 machine. The experimental conditions were identical to those described in Reference 7 and resulted in a voxel size of 9.9 μm for the full samples and 2.0 μm for the machined cylinder. Standard HIPing conditions were subsequently applied to all the samples, involving a temperature of 1193 K (920 °C) combined with a pressure of 100 MPa (applied *via* argon gas) for 2 hours, followed by cooling to room temperature at a rate of 6 ± 2 K/min. After HIPing, the samples were subjected to a second XCT scan with identical settings and position indexing was employed so that individual defects could be re-imaged.

The XCT data were reconstructed into 3D volumes using a filtered back projection algorithm and imported into Avizo Fire 8 for analysis. After HIPing, the image registration tool in the Avizo software was used to exactly re-align the datasets, using a least squares method to match their gray levels, allowing direct comparison of the same sample slices. It should be noted that although in XCT the voxel size is fixed by the experimental setup, the resolution (the smallest feature perceptible from the reconstructed 3D voxel data) is still influenced by the ability to differentiate features from their absorption difference, while avoiding false-positive identification of noise in the data. Noise can be introduced in a number of ways, including scatter of X-ray photons within the sample, beam hardening, incorrect determination of the center of rotation during reconstruction, mechanical errors from stage movement, and blurring from a finite rather than point X-ray source. A more thorough discussion of these factors and their effect on resolution is available elsewhere.[17,18] Quantification of the data from both the as-built and HIPed condition was conducted by first segmenting it into solid and void using the Otsu method to calculate the optimum global threshold.[19] To account for any noise in the segmented data, islands of less than 2^3 (8) voxels were not included in any quantification of overall pore volume fractions or individual pore sizes. This method allowed pores with an equivalent diameter greater than 24.6 and 5.2 μm to be identified, without any subjective choice of threshold, using automatic segmentation of the full sample and machined cylinder datasets, respectively.

Example 3D visualizations of the pores (shown in red) detected in the full-sample scans of geometries C1 and T3, in the as-built condition and following HIPing, are shown in Figure 2. The most striking features in the pre-HIP visualizations of these samples are the large tunnel defects seen in sample T3. These tunnel defects were observed in all the samples except C1. They tended to be located approximately 1 mm in from the samples' surfaces, which is at the edge of the hatching area, and consisted of branched tunnels with a typical diameter between 200 and 600 μm that grew vertically through many deposited layers. Their presence at the edge of the hatching region is indicative of too low a line energy being applied in this region by the old control software during beam turning.[10] Prior work[6] has shown that a greater density of defects occurs at the edge of the

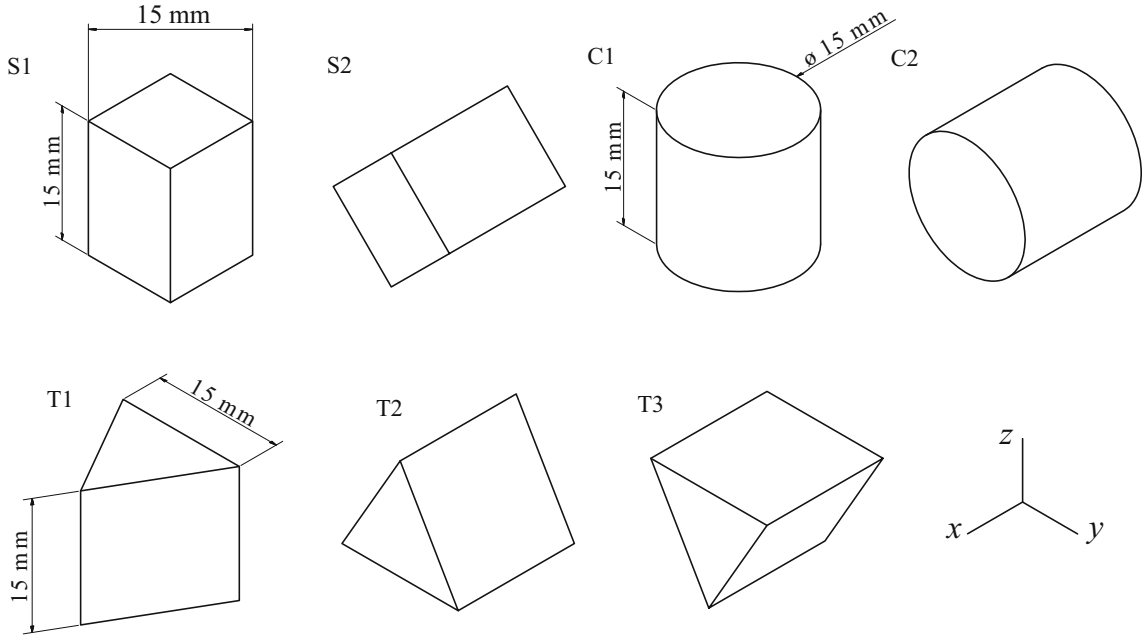

Fig. 1—Geometries and designations of the samples used to investigate the effect of HIPing on defect populations. The reference system denotes the orientation of the two orthogonal hatching directions (x and y) and the build direction (z).

hatching region because it receives too low an energy density, due to the turning function increasing the beam traverse speed too much when the beam turns back on itself. The maximum decrease in line energy caused by this effect occurs at the very edge of the hatching region, where the tunnels defects were observed. In samples with overhanging features (such as T3 in Figure 2) the 'thickness function,' which is designed to reduce energy density where melting is required directly above the lower conductivity powder bed, will further increase the beam speed, exacerbating the generation of edge-of-hatch tunnel defects.

More conventional defects, such as smaller gas pores and lack of fusion defects, were also visible in all samples, examples of which are shown in the views from the high-resolution scan in Figure 2. With sample C1, it can be seen by comparison of the images in Figure 2 and the net pore volume fraction data presented in Table I that all the detectable internal porosity present after AM was removed by the HIPing treatment. In contrast, while all the smaller gas porosity in sample T3 was removed by HIPing, some tunnel defects still persisted in the HIPed samples.

Prior to analysis of the post-HIP XCT results, the datasets were exactly aligned with the data collected from the samples in the as-built condition, with respect to the sample dimensions. Thus, the example slices compared in Figure 4, from geometries C2 and T3, show the same internal slice of each sample before and after HIPing. In Figure 3(a), it can be seen that even the coarse tunnel defects have all been removed from the cylindrical sample, whereas in Figure 3(b), which had an inverted prism geometry, some remain. Detailed examination of individual slices revealed that all the tunnel defects remaining after HIPing in sample T3 were connected by ligaments to the surface. Somewhat surprisingly, the measured volume of the tunnel defects that remained following HIPing had actually increased by approximately 4 to 7 pct. In contrast, porosity completely enclosed by solid material was healed below the XCT detection limit following HIPing; *i.e.*, it had shrunk in size to below the resolution of the equipment.

The average volume fraction of porosity detected by automatic segmentation of the as-built and HIPed samples is shown in Table I. In all cases, the detected pore volume fractions had reduced following the HIP cycle. In sample geometries S2, C1, C2, and T2, this was to below the detectable limit of the coarse scan. The only detectable pores that persisted after the HIP cycle were the large tunnel defects that were found to have breached the top surface of the samples. Only the samples with a top surface melted by the hatching strategy had this open porosity present after HIPing (*i.e.*, S1, T1, and T3). In contrast, tunnel defects present in samples built where the upper surface had been melted with the contour strategy (such as S2, C2, and T2) were not connected to the surface and were closed by the HIPing process, despite the similar coarse nature of the original flaws. All of these samples showed no detectable porosity following HIPing at the 24.6-μm resolution limit of the full-sample scan.

To see if the flaws in these samples were fully healed, high-resolution XCT examination of the small cylindrical specimen machined from the edge of a cuboid sample was carried out. This again revealed no internal pores that could be detected following HIPing, either by automatic segmentation or manual examination of the data. High-resolution example slices from the machined cylinder are provided in Figure 4, again showing the same regions before and after HIPing. It can be seen

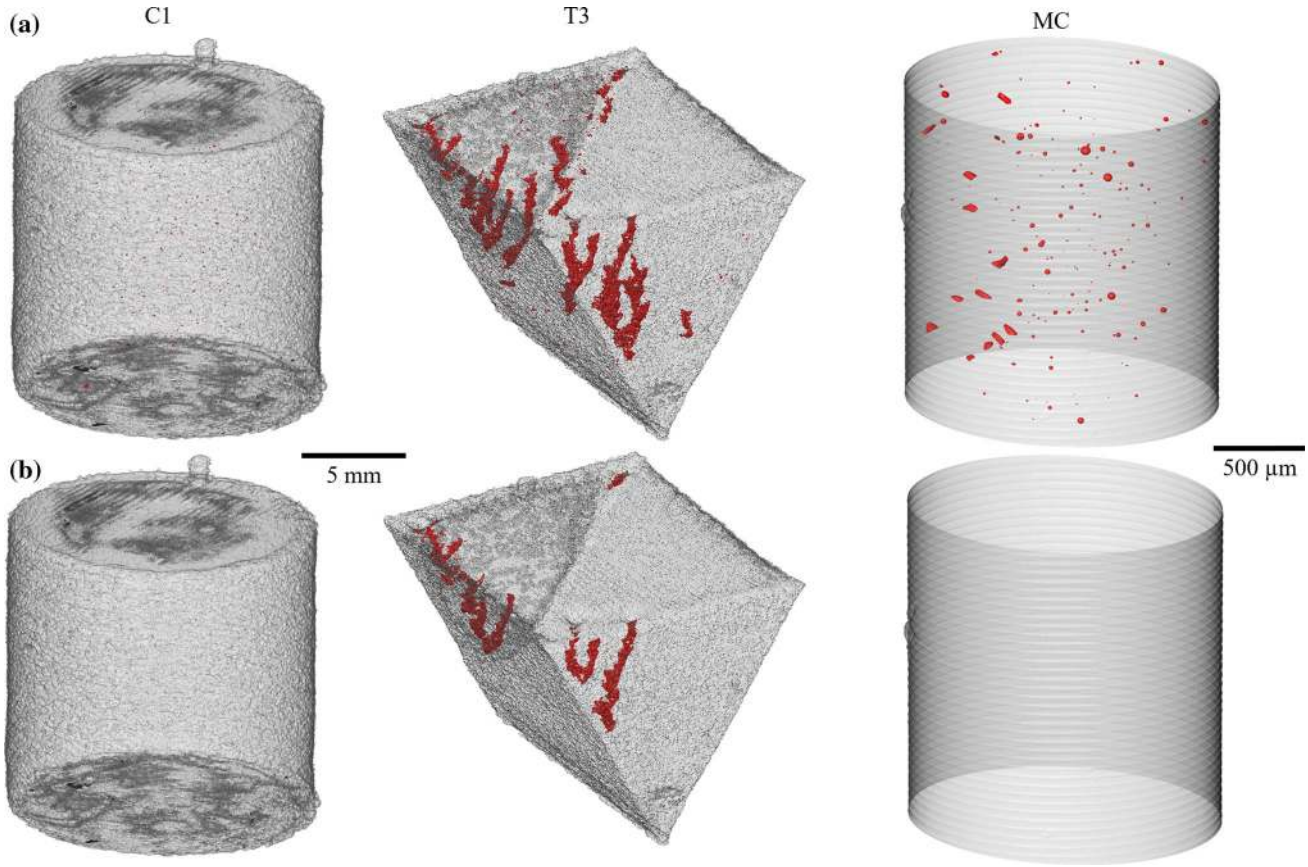

Fig. 2—Isometric 3D visualization of defects (red) in samples C1 and T3, and in the high-resolution scan of the edge of a cuboid sample (labeled MC): (*a*) as-built; and (*b*) after HIPing. All internal porosity was removed in samples C1 and MC, following HIPing, whereas in sample T3, tunnel defects connected to the surface persisted. The build direction for all samples is vertical.

Table I. Pore Volume Fractions Measured by XCT of the Full SEBM Ti-6Al-4V Samples with the Different Geometries Shown in Fig. 1, S1-T3 and from the Higher Resolution Scans of the Small Cylinder Edge (MC) of a Cuboid Sample, As-Built and After a HIP Cycle

Sample	Voxel Size (μm)	Pore Volume Fraction (%)		Percentage Reduction in Pore Volume Fraction
		As-Built	Post-HIP	
S1	9.9	0.260	0.064	75
S2		0.202	0.000	100
C1		0.001	0.000	100
C2		0.195	0.000	100
T1		0.625	0.197	68
T2		0.118	0.000	100
T3		0.225	0.062	72
MC	2.0	0.041	0.000	100

that the two conventional pores types initially present, a spherical gas pore (Figure 4(a)) and a lack of fusion defect (Figure 4(b)), are both undetectable in the XCT data acquired following HIPing.

The results presented have thus shown HIPing to be very effective in closing porosity contained within Ti-6Al-4V components, manufactured by SEBM-AM. This in itself is unsurprising, given the success HIPing has enjoyed when applied to Ti-6Al-4V castings.[11,13] However, the large tunnel defects, which could appear as separated segments in the 3D visualizations of the XCT data due to the small size of the ligaments connecting them, were found to persist in some samples following the HIPing process. When this occurred, more careful manual analysis (*e.g.*, Figure 3) revealed that in all cases these flaws were connected to the top surface of the build and this would allow the infiltration of the pressurized argon gas into the tunnel cavity during HIPing, preventing it closing. In fact, HIPIng appears to have led to a slight expansion in the volume measured

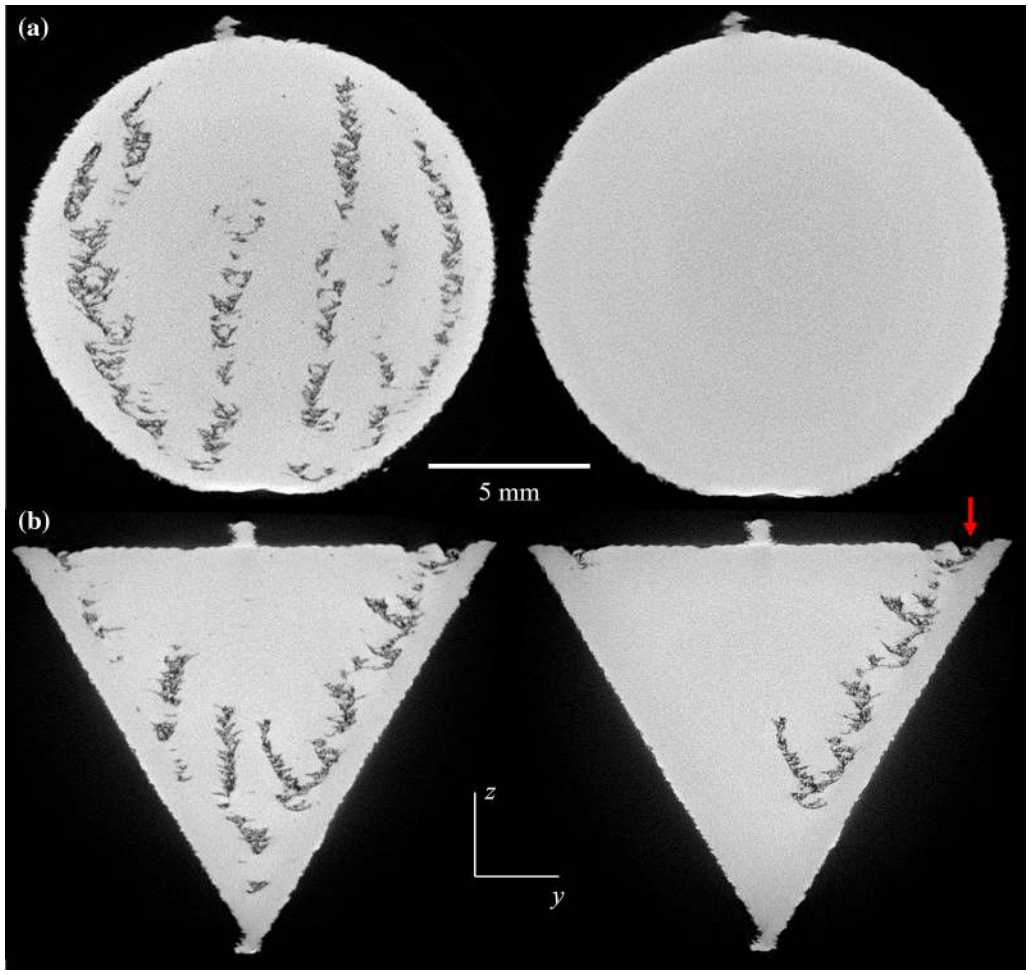

Fig. 3—Examples of aligned vertical internal (x–z) slices from XCT data collected as-built (left) and after HIPing (right) in samples: (*a*) C2 and (*b*) T3. In (b) note the tunnel defects that breach the surface (arrowed) that are still present after HIPing. The build direction for both samples is vertical in the plane of the page.

for these large defects. This could be because infiltration of argon under high pressure may have led to an expansion of these defects at the expensive of internal porosity that was present in close proximity, or it may be caused by a measurement effect, in that if the tunnel defects surfaces became smoother during the HIPing heat treatment, this could increase the volume that is segmented in the XCT data. The potential of these large, high-aspect ratio defects to have a detrimental effect on the mechanical properties of SEBM samples is thus aggravated by the failure of HIPing to close those that were open to the surface. However, surface connected pores in traditionally manufactured components can be removed by the application of a coating prior to HIPing, which effectively makes the porosity internal.[12]

It is important to note that, because of its large atomic diameter, argon cannot diffuse readily through titanium. Indeed, argon is the gas used to exert pressure during HIPing.[12] Hence, if the gas pores in SEBM components are caused by argon bubbles, it would be expected that they could persist in the sample after HIPing, all be it at a significantly smaller size and a much higher internal pressure. In contrast, when HIPing gas porosity in castings, which is typically caused by hydrogen contamination, it is assumed that the gas is soluble and can thus diffuse out of the casting.[12] It is therefore interesting to estimate the increase in pressure that would be expected within the gas pores as they shrink to below the detection limit in XCT after HIPing. To estimate the initial pressure within the gas pores, following SEBM, first, the hydrostatic pressure (P_h) in a liquid can be calculated from

$$P_h = P_{atm} + \rho \cdot g \cdot h, \qquad [1]$$

where P_{atm}, ρ, g, and h are the atmospheric pressure (0.1 Pa in the vacuum chamber), the density of the liquid (4123 kg m^{-3} for the Ti-6Al-4V melt), gravitational acceleration (9.81 m s^{-2}), and depth, respectively. Using the depth of the melt pool (150 μm)[2] as a reasonable estimate of the maximum depth possible below the melt pool surface, the hydrostatic pressure will be 6.2 Pa, which is negligible in comparison to the HIPing pressure of 100 MPa. Within a bubble, the pressure is further increased by the surface energy of the interface between the gas and liquid (γ = 1.52 J m^{-2} for liquid titanium).[20]

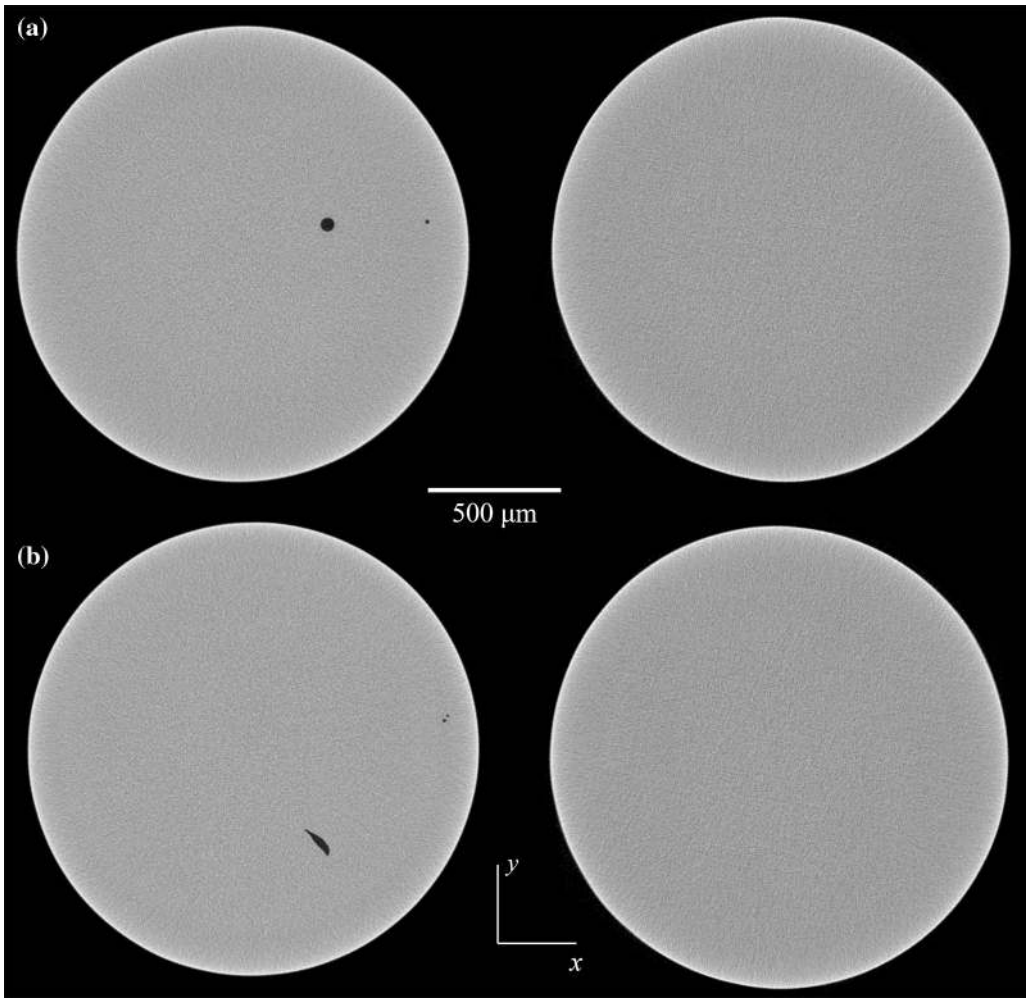

Fig. 4—Examples of aligned slices of high-resolution XCT data collected from the cylindrical sample machined from a cuboid sample prior to (left) and after the HIP cycle (right). Showing a: (*a*) large gas pores; and (*b*) a lack of fusion defect. The build direction for both is perpendicular to the plane of the page.

The pressure increase (ΔP) is a function of the radius of curvature of the bubble (r), and for a spherical bubble is given by

$$\Delta P = 2 \cdot \gamma / r. \quad [2]$$

Thus, the as-built pressure within the gas pores detected can be estimated as $P = P_h + \Delta P$. For example, the pressure within the largest gas pore detected by high-resolution XCT, which had a diameter of 52 μm, can be estimated to be ~120 kPa, whereas the largest detected by the lower resolution XCT, which had a diameter of 170 μm and was located in sample T1, would have an initial internal pressure of ~40 kPa. The temperature within the bubbles was assumed to be equal to the solidus temperature of Ti-6Al-4V, 1877 K (1604 °C). Disregarding any transient effects, the change in pressure (P) due to the temperature and volume changes experienced during HIPing can then be approximated using the ideal gas law:

$$P \cdot V = n \cdot R \cdot T, \quad [3]$$

where V, n, R, and T are the volume (m^3), number of moles, universal gas constant (8.314 J K^{-1} mol^{-1}), and temperature (K), respectively. Here, we assume that the number of moles remains constant due to the lack of diffusion of argon atoms in solid titanium and hence the ratio $P{\cdot}V/T$ is equal to a constant. The constant temperature during HIPing (1193 K) thus allows the relationship between pressure and volume to be calculated and this is shown in Figure 5 for the two largest gas pores detected. It is clear that, according to this simplistic model, the pressure within the gas pores increases substantially as they shrink in volume, but both the pores will still reduce below the detectability limit of the equipment before they reach equilibrium with the 100 MPa HIPing pressure. While the ideal gas law applied here is unlikely to result in the true value of the pressure change, this rough estimate highlights both the large increase in pressure that could

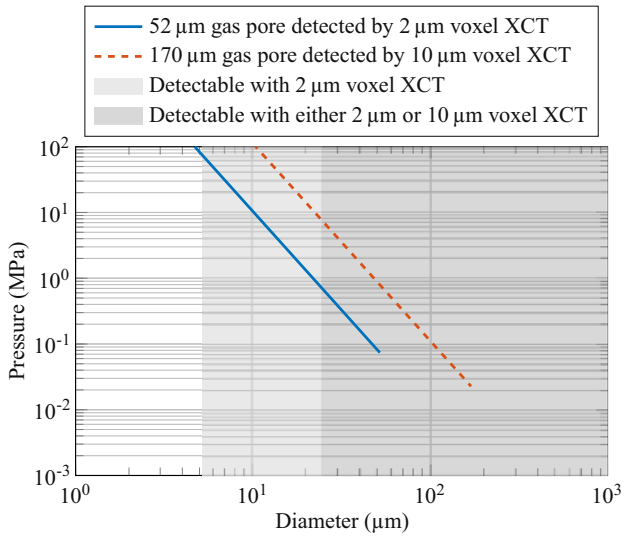

Fig. 5—Pressure increase due to shrinkage of the largest gas pores detected by high- and low-resolution XCT estimated with the ideal gas law. The detection limits of the XCT equipment are indicated by the background color.

result as the pores shrink and that the pores will ultimately reach a volume where they cease to shrink under the application of a constant pressure, which is dependent on their as-built volume. The calculated size of the gas pore at the equilibrium pressure (100 MPa) was only a small way below the detection limit of the XCT equipment used (5 μm), indicating that if a higher resolution system had been used, or larger gas pores been detected initially, some remnant of the pores may have been detectable following the HIP cycle. In addition, in other AM processes conducted under a shielding gas, rather than a vacuum chamber, such as selective laser melting (SLM), the pressure within the as-built pores could be much higher. HIPing may therefore be less effective when applied to components manufactured *via* these AM systems.

Nonetheless, the high-cycle fatigue life of Ti-6Al-4V samples manufactured by SEBM has been shown to be greatly improved following a HIP cycle.[14,15] High-cycle fatigue is generally dominated by the number of cycles required to initiate a crack,[21] so the removal of ready crack initiation sites is the primary reason behind the increase in fatigue life. The size of a spherical pore does not, in fact, change its stress concentration factor,[3] but of importance in determining fatigue initiation is the effect of a reduction in the size of the plastic zone near a defect relative to the scale of microstructural barriers to early stage crack growth.[21] It has been shown here that any remaining argon filled pores would be less than 5 μm in diameter, and this would increase the stress concentration in only a very small volume of material above the elastic limit. Such tiny pores are hence unlikely to initiate a crack able to break through microstructural barriers such as α colony boundaries.[21] The microstructural coarsening that occurs in high-temperature HIPing cycles, and associated increase in crack propagation resistance, has also been suggested as a reason for the increase in fatigue strength seen in Ti-6Al-4V SEBM components following HIPing.[15] While this may increase the crack propagation resistance and reduce the smaller crack propagation contribution to high fatigue life, it seems more likely that the reduction in pore size caused by HIPing is the major reason for the improvement observed, given the reasoning and results outlined above.

In summary, HIPing has been confirmed to be an effective method to remove gas pores, lack of fusion defects, and even large scale internal porosity, from worst-case AM components built under non-optimized conditions. However, surface connected porosity was found to be retained, and possibly expanded after HIPing. Comparison of samples built with different geometries revealed that such flaws were exclusively large tunnel defects present in builds which had a top surface melted by the hatching strategy. Even at high resolutions, no evidence of conventional internal (gas) porosity could be observed in the HIPed samples by XCT; therefore, any residual voids can be assumed to have collapsed to below the resolution limit of the equipment, which was approximately 5 μm.

Thanks to Camille Kayode Agbanrin and Fabien Leonard for assistance with data processing. The authors acknowledge EPSRC funding from: the CDT in Metallic Systems (EP/G036950/1), the designing alloys for resource efficiency (DARE) program (EP/L025213/1) and the Henry Moseley X-ray Imaging Facility under EP/F007906/1, EP/F001452/1 and EP/M010619/1. For access to the original data please contact the corresponding author.

OPEN ACCESS

REFERENCES

1. P. Edwards, A. O'Conner, and M. Ramulu: *J. Manuf. Sci. Eng.*, 2013, vol. 135, p. 061016–061016-7, DOI:10.1115/1.4025773.
2. A.A. Antonysamy: PhD Thesis, University of Manchester, 2012. https://www.escholar.manchester.ac.uk/uk-ac-man-scw:160535.
3. W.D. Pilkey and D.F. Pilkey: *Peterson's Stress Concentration Factors*, 3rd ed., Wiley, Hoboken, 2008.
4. S.M. Gaytan, L.E. Murr, F. Medina, E. Martinez, M.I. Lopez, and R.B. Wicker: *Mater. Technol. Adv. Perform. Mater.*, 2009, vol. 24, pp. 180–90, DOI:10.1179/106678509X12475882446133.

5. J. Karlsson, A. Snis, H. Engqvist, and J. Lausmaa: *J. Mater. Process. Technol.*, 2013, vol. 213, pp. 2109–18, DOI: 10.1016/j.jmatprotec.2013.06.010.
6. N. Hrabe and T. Quinn: *Mater. Sci. Eng. A*, 2013, vol. 573, pp. 271–77, DOI:10.1016/j.msea.2013.02.065.
7. S. Tammas-Williams, H. Zhao, F. Léonard, F. Derguti, I. Todd, and P.B. Prangnell: *Mater. Charact.*, 2015, vol. 102, pp. 47–61, DOI:10.1016/j.matchar.2015.02.008.
8. K. Puebla, L.E. Murr, S.M. Gaytan, E. Martinez, F. Medina, and R.B. Wicker: *Mater. Sci. Appl.*, 2012, vol. 3, pp. 259–64, DOI: 10.4236/msa.2012.35038.
9. N. Hrabe and T. Quinn: *Mater. Sci. Eng. A*, 2013, vol. 573, pp. 264–70, DOI:10.1016/j.msea.2013.02.064.
10. A. Bauereiß, T. Scharowsky, and C. Körner: *J. Mater. Process. Technol.*, 2014, vol. 214, pp. 2497–504, DOI:10.1016/j.jmatprotec.2014.05.002.
11. G. Lütjering and J.C. Williams: *Titanium*, 2nd ed., Springer, Berlin, 2007.
12. H. Atkinson and S. Davies: *Metall. Mater. Trans. A*, 2000, vol. 31A, pp. 2981–3000, DOI:10.1007/s11661-000-0078-2.
13. A. du Plessis and P. Rossouw: *J. Mater. Eng. Perform.*, 2015, vol. 24, pp. 3137–41, DOI:10.1007/s11665-015-1580-4.
14. W.E. Frazier: *J. Mater. Eng. Perform.*, 2014, vol. 23, pp. 1917–28, DOI:10.1007/s11665-014-0958-z.
15. L. Facchini, E. Magalini, P. Robotti, and A. Molinari: *Rapid Prototyp. J.*, 2009, vol. 15, pp. 171–78, DOI: 10.1108/13552540910960262.
16. C.J. Smith, F. Derguti, E.H. Nava, M. Thomas, S. Tammas-Williams, S. Gulizia, *et al.*: *J. Mater. Process. Technol.*, 2016, vol. 229, pp. 128–38, DOI:10.1016/j.jmatprotec.2015.08.028.
17. E. Maire and P.J. Withers: *Int. Mater. Rev.*, 2013, vol. 59, pp. 1–43, DOI:10.1179/1743280413Y.0000000023.
18. S.R. Stock: *Int. Mater. Rev.*, 2008, vol. 53, pp. 129–81, DOI: 10.1179/174328008X277803.
19. N. Otsu: *IEEE Trans. Syst. Man. Cybern. SMC*, 1979, vol. 9, pp. 62–66, DOI:10.1109/TSMC.1979.4310076.
20. H.M. Lu and Q. Jiang: *J. Phys. Chem. B*, 2005, vol. 109, pp. 15463–68, DOI:10.1021/jp0516341.
21. S. Suresh: *Fatigue of Materials*, 1st ed., Cambridge University Press, Cambridge, 1991.